Large-Signal Equivalent Circuit for Datacom VCSELs

Citation for the original published paper (version of record):

Grabowski, A., Gustavsson, J., He, Z. et al (2021). Large-Signal Equivalent Circuit for Datacom
VCSELs. Journal of Lightwave Technology, 39(10): 3225-3236.
http://dx.doi.org/10.1109/JLT.2021.3064465

N.B. When citing this work, cite the original published paper.

(article starts on next page)

Large-Signal Equivalent Circuit for Datacom VCSELs

Alexander Grabowski, *Student, IEEE,* Johan Gustavsson, Zhongxia He, *Senior Member, IEEE,*
and Anders Larsson, *Fellow, IEEE*

Abstract—Increasing the baud rate in optical interconnects (OIs) will require the use of more sophisticated driver and receiver electronics. This will help overcome the stagnated bandwidth of the Vertical-Cavity Surface-Emitting Laser (VCSEL) and the pin-photodetector. Next generation OIs operating at single lane rates of 50+ Gbaud will therefore require careful co-optimization of the electronics and the optoelectronics. To facilitate this work there is a need of an accurate equivalent circuit for the optoelectronic components, functioning over a broad drive current and ambient temperature range. The VCSEL is the most important and complex to model due to its non-linear behavior and strongly varying characteristics with drive current and ambient temperature. For this purpose, a large-signal equivalent circuit dedicated for high-speed datacom VCSELs has been developed and is presented here. The distributed electrical parasitics in the device layout are carefully considered, the intrinsic speed limitation from carrier transport effects in the Separate-Confinement-Heterostructure (SCH) and the carrier-photon interaction in the Quantum Wells (QWs) are included, and self-heating effects in the device are monitored. The circuit is purposely based on physical instead of empirical models so that it can provide usable feedback to VCSEL designers. For circuit demonstration, it is implemented in Keysight's Advanced Design System (ADS) software and thereafter applied to replicate the performance of a state-of-the-art 28-GHz-bandwidth VCSEL at different temperatures and drive currents. Comparison is made between simulated and measured steady-state characteristics, small-signal behavior, and large-signal response under 28 Gbaud On-Off-Keying (OOK) and Pulse-Amplitude-Modulation 4 (PAM4) modulation, showing good agreement.

Index Terms—Data communication, Equivalent circuits, Semiconductor device modeling, Semiconductor lasers.

I. INTRODUCTION

Optical Interconnects (OIs) are heavily employed in datacenters and high-performance computing systems for connecting computational, storage, and switch units. The OIs are predominantly based on uncooled GaAs-based Vertical-Cavity Surface-Emitting Lasers (VCSELs), multimode optical fibers, and pin-photodetectors as this provides the most cost and energy effective solution [1]. Today, the single lane rate of commercial OIs is up to 28 Gbaud, using On-Off-Keying (OOK) or Pulse-Amplitude-Modulation 4 (PAM4) modulation,

and in the next generation it will increase to 50+ Gbaud [2]. The development of OIs with such high single lane rates is, however, obstructed by the stagnation in improving the bandwidth of datacom VCSELs and pin-detectors, to exceed $\sim$30 GHz. The focus has therefore been shifted to utilize more sophisticated driver and receiver electronics to be able to compensate for the limited bandwidth of the optoelectronic components. This includes the use of pre-emphasis in the driver electronics and equalization in the receiver electronics, as demonstrated for example by [3]. But to optimize performance and minimize power consumption for more complex OIs it becomes essential to co-design the driver and receiver electronics with the VCSEL and pin-photodetector. Electronic designers are therefore requesting accurate equivalent circuits for the VCSEL and pin-photodetector, that can predict their performance at varying ambient temperatures and currents. To allow for the co-design, the equivalent circuits need to have circuit elements that are directly linked to parameters in, or extracted from, the 2D/3D physics-based optical-electrical-thermal modelling tools that the VCSEL and pin-photodetector designers use. Via, for example, a circuit element sensitivity analysis the electronic designer can then provide feedback on critical parameters that needs to be improved. With the above in mind, the VCSEL is the most sensitive component of the OI, with performance that varies considerably with ambient temperature and drive current.

Therefore, in this work we have developed an equivalent circuit for high-speed datacom VCSELs that can be used to predict the performance at ambient temperatures between room temperature and 75°C and for drive currents ranging from below the threshold current and up to the thermal rollover. It accounts, for example, for the input impedance mismatch, optical output power saturation from self-heating, and intrinsic speed limitation from carrier transport effects in the Separate-Confinement-Heterostructure (SCH). The equivalent circuit consists of five interdependent sub-circuits. The first sub-circuit models the device input impedance and the voltage drop over SCH region and the second and third sub-circuits model the free carrier accumulation above the barriers and in the Quantum Wells (QWs), respectively, in the SCH. In this way, the important carrier capture dynamics for the QWs via relaxation from continuum states to bound states can be accounted for. The fourth sub-circuit models the photon accumulation in the optical resonator from stimulated emission, where a fraction of these photons escapes through the top mirror to produce the useful output power. The fifth sub-circuit is used to track the internal device temperature via

a thermal impedance model, accounting both for self-heating and ambient temperature effects. The focus of the work has been to have the model treat the non-linear dynamic response of the VCSEL with such precision that it is able to accurately reproduce the optical waveforms generated by the VCSEL under different modulation conditions. Further developments of the model will involve adding the frequency dependent intensity noise.

This work is an extension of [4] and examples of recent similar works on this topic can be found in [5], [6], [7], [8]. This work together with [5] include the additional use of two sub-circuits to keep track of the free carriers in the barrier regions and in the QWs. This allows for the inclusion of the finite time it takes for the carriers to be captured by the QWs. This carrier transport effect is well known to affect the modulation speed of semiconductor lasers [9]. Our work however differs to work [5] in that we employ a different sub-circuit for modelling the input impedance and voltage drop over the SCH region. For the latter we use a voltage source instead of passive circuit elements, where voltage is calculated from quasi-Fermi levels and free carrier concentrations in the QWs and above the barriers. In this way, the sub-circuit becomes an active circuit that is interdependent on the other sub-circuits, making it possible to model the non-linear steady-state current-voltage characteristics for the VCSEL based on physics (via quasi-Fermi level calculations), and also have a physics-based (instead of empirical) diffusion capacitance that connects to the VCSEL design, both for improved feedback to VCSEL designers. By also including more temperature dependent parameters, supplied by the VCSEL designers, the equivalent circuit is shown usable for a wide range of ambient temperatures (instead of only room temperature as in [5]).

A few examples of transmission experiments for 50+ Gbps datacom applications, where a model such as ours could be beneficial as an optimization tool, can be found in [10], [11] and [12].

The paper is organized as follows, in section II the VCSEL equivalent circuit model is presented together with underlying physical models and related material and device parameters. In section III the circuit is demonstrated for a state-of-the-art 28-GHz-bandwidth VCSEL. Simulated characteristics is compared to measured data, including current-voltage-optical output power, wavelength shift with current, frequency dependent S_{11}- and S_{21}-parameters, and large-signal time-response under 28 Gbaud OOK and PAM4 modulation. Finally, conclusions are given in section IV.

II. LARGE-SIGNAL VCSEL EQUIVALENT CIRCUIT

The large-signal equivalent circuit for the VCSEL is intended for high-speed directly modulated GaAs-based VCSELs for datacom applications. It consists of five interdependent sub-circuits as shown in Fig. 1, which are individually explained in the following sub-sections. At the input, the current I [A] and the voltage U [V] represent the VCSEL drive current and VCSEL voltage drop, respectively. At the output, the current I_{tm} [A] provides the optical output power from the VCSEL, P_{opt} [W], i.e. $I_{tm} \sim P_{opt}$.

A. Sub-Circuit 1: Input Impedance and Voltage Drop

Sub-circuit 1 is used to model the VCSEL's input impedance and the voltage drop over the SCH. The input impedance is important as it determines e.g. the impedance mismatch to the driver, and the parasitic low-pass filtering of the electrical signal applied to the VCSEL. The input impedance is modelled by a passive circuit containing resistors, inductors, and capacitors. As the input impedance depends strongly on the layout of the device, e.g. mesa structure, multiple oxide structures, proton implantation schemes, pad design etc., the passive circuit needs to be carefully adapted to the particular VCSEL design, and an example is given for the demonstration case in section III. Resistors used for representing the mesa resistance are set to be temperature dependent, as they are much affected by the ambient temperature and the self-heating in the VCSEL.

The voltage drop over the SCH, U_{SCH} [V], depends on the quasi-Fermi level separation in the SCH, which in turn depends on the free carrier concentration and temperature. The number of free carriers in the bound (ground) states of the QWs, n_A, and in the continuum states above the barriers, n_B, are treated as separate equilibrium pools (separate quasi-Fermi levels). As the model traces both of these pools of carriers, the voltage U_{SCH} is calculated by a weighted average based on carrier energy:

$$U_{SCH}(I_{SCH}, T) \approx$$
$$\frac{n_A \cdot E_{f,A}(n_A, T) + n_B \cdot E_{f,B}(n_B, T)}{q \cdot (n_A + n_B)}, \quad (1)$$

where q is the elementary charge, T is the internal temperature, and $E_{f,A}$ and $E_{f,B}$ are the quasi-Fermi level separations in the QWs (n_A pool) and above the barriers of the SCH (n_B pool), respectively. The quasi-Fermi levels are computed via [9], [13]:

$$E_{f_A}(n_A, T) = E_{g,A}(T) +$$
$$\eta_A \cdot \sum_{i=e,hh} k \cdot T \cdot \ln\left[\exp\left(\frac{h^2 \cdot d_{QW} \cdot n_A/V_A}{4\pi \cdot k \cdot T \cdot m_0 \cdot m_{i,A}}\right) - 1\right],$$
$$(2)$$

$$E_{f_B}(n_B, T) = E_{g,B}(T) + \eta_B \cdot \sum_{i=C,V} k \cdot T \cdot \left[\frac{\ln\left(\frac{n_B/V_B}{N_i(T)}\right)}{1 - \left(\frac{n_B/V_B}{N_i(T)}\right)^2} + \frac{\left(\frac{3\sqrt{\pi} \cdot n_B/V_B}{4 \cdot N_i(T)}\right)^{2/3}}{1 + \left[0.24 + 1.08 \cdot \left(\frac{3\sqrt{\pi} \cdot n_B/V_B}{4 \cdot N_i(T)}\right)^{2/3}\right]^{-2}}\right], \quad (3)$$

where the conduction and valence band effective density of states in the continuum above the barriers, N_C and N_V, respectively, are given by:

$$N_C(T) = 2 \cdot \left(\frac{2\pi \cdot m_0 \cdot m_{e,B} \cdot k \cdot T}{h^2}\right)^{3/2}, \quad (4)$$
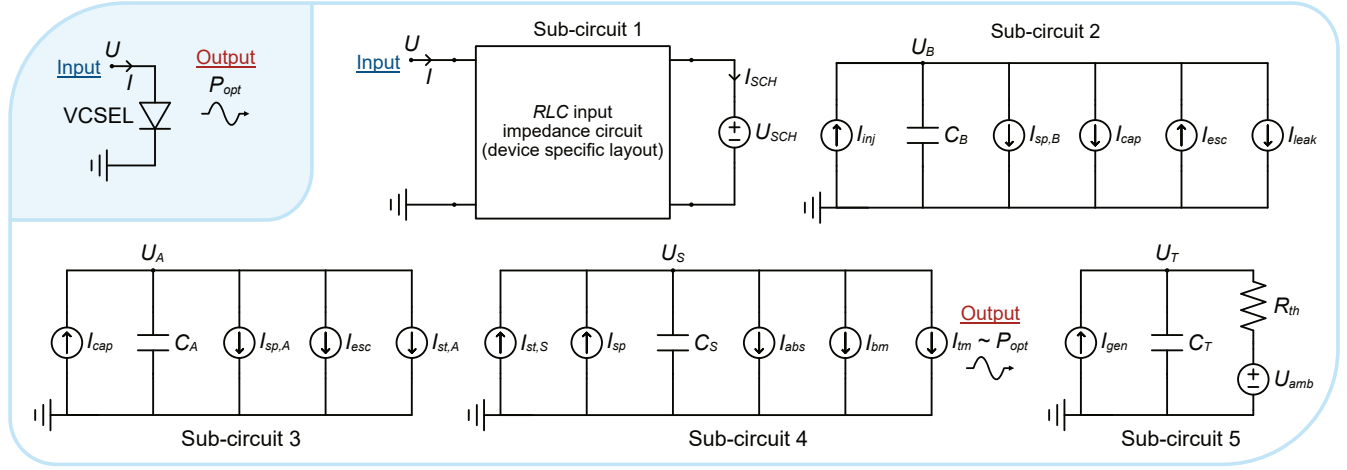
Fig. 1. Equivalent circuit for a high-speed datacom VCSEL.

$$N_V(T) = 2 \cdot \left(\frac{2\pi \cdot m_0 \cdot m_{hh,B} \cdot k \cdot T}{h^2} \right)^{3/2} . \quad (5)$$

Note that only the lowest sub-band of the QWs is considered when computing E_{f_A}. $E_{g,A}$ is the band gap of the QWs including the quantization energy, $E_{g,B}$ is the band gap of the barrier region, d_{QW} is the QW thickness, k is Boltzmann's constant, h is Planck's constant, m_0 is the free electron mass, $m_{e,A}$ and $m_{hh,A}$ are the relative electron and hole effective mass in the QWs, and $m_{e,B}$ and $m_{hh,B}$ are the relative electron and hole effective mass in the continuum. η_A and η_B are ideality factors (i.e. ≥ 1) for the QWs and barrier regions, respectively, to account for a non-ideal crystal quality. V_A and V_B are the volumes of the QWs and barrier regions, respectively, and calculated as:

$$V_A = d_A \cdot A_{aperture} \quad (6)$$
$$V_B = d_B \cdot A_{aperture} \quad (7)$$

where d_A is the total thickness of the QWs (number of quantum wells, n_{QW}, multiplied by their thickness, i.e. $d_A = n_{QW} \cdot d_{QW}$), d_B is the total thickness of the barrier region (as defined in Fig. 2), and $A_{aperture}$ is the area to which the injected current is laterally confined in the SCH.

B. Sub-Circuit 2 and 3: Charge Accumulation in SCH

Sub-circuits 2 and 3 are used to trace the number of free carriers accumulated in the SCH, where sub-circuit 2 keeps track of the free carriers in the barrier region continuum states, n_B, and sub-circuit 3 keeps track of the free carriers in the bound (ground) states of QWs, n_A. This allows for accounting for the effects of carrier transport processes (injection, capture, emission, leakage) on VCSEL dynamics, see Fig. 2. Charge neutrality is assumed so that n_A and n_B represent both the free electrons in the conduction band and the free holes in the valence band in the QWs and continuum, respectively.
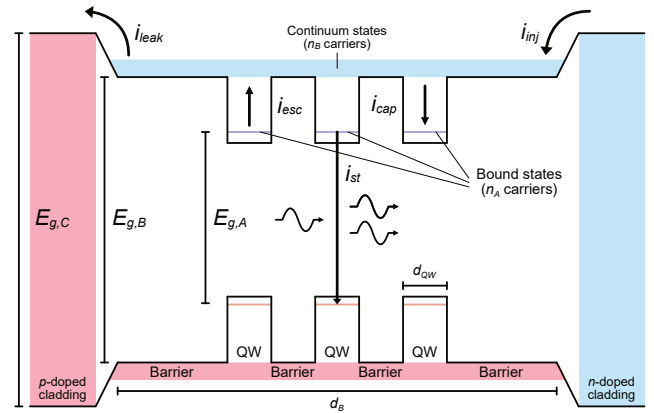

Fig. 2. Energy band diagram of the SCH and its cladding along the vertical direction in the VCSEL, with free carrier (free electron) flows for injection, capture, stimulated emission, escape, and leakage. The band gaps in the different regions (claddings, barriers, and QWs) are also indicated, as well as the thickness of the QWs and the barrier region.

The following two coupled rate equations are used to describe the change in n_B and n_A with time, similar to [9], [14]:

$$\frac{dn_B}{dt} = i_{inj} - i_{sp,B} - i_{cap} + i_{esc} - i_{leak}, \quad (8)$$
$$\frac{dn_A}{dt} = i_{cap} - i_{sp,A} - i_{esc} - i_{st}, \quad (9)$$

where i_{inj} is the carrier injection rate into the SCH (within $A_{aperture}$), $i_{sp,B}$ is the spontaneous carrier recombination rate in the barrier region, i_{cap} is the QW carrier capture rate, i_{esc} is the QW carrier escape rate, i_{leak} is the SCH carrier leakage rate, $i_{sp,A}$ is the spontaneous carrier recombination rate in the QWs, and i_{st} is the stimulated carrier recombination rate in

the QWs. These rates are in turn modelled by:

$$i_{inj} = \eta_{inj,xy} \cdot \frac{I_{SCH}}{q}, \tag{10}$$

$$i_{sp,B}(n_B) = \frac{n_B}{\tau_{sp,B}}, \tag{11}$$

$$i_{cap}(n_B) = \frac{n_B}{\tau_{cap}}, \tag{12}$$

$$i_{esc}(n_A,T) = \frac{A_{0,A} \cdot V_A \cdot T^2}{q \cdot d_A} \cdot \exp\left(-\frac{E_{g,B}(T)}{\eta_{esc} \cdot k \cdot T}\right) \cdot \left[\exp\left(\frac{E_{f,A}(n_A,T)}{\eta_{esc} \cdot k \cdot T}\right) - 1\right], \tag{13}$$

$$i_{leak}(n_B,T) = \frac{A_{0,B} \cdot V_B \cdot T^2}{q \cdot d_B} \cdot \exp\left(-\frac{E_{g,C}(T)}{\eta_{leak} \cdot k \cdot T}\right) \cdot \left[\exp\left(\frac{E_{f,B}(n_B,T)}{\eta_{leak} \cdot k \cdot T}\right) - 1\right], \tag{14}$$

$$i_{sp,A}(n_A,T) = A(T) \cdot n_A + B(T) \cdot \frac{n_A^2}{V_A} + C(T) \cdot \frac{n_A^3}{V_A^2} \tag{15}$$

$$i_{st}(n_A,S,T) = \Gamma \cdot \nu_g \cdot g(n_A,S,T) \cdot S, \tag{16}$$

where I_{SCH} is the current reaching the SCH, $\eta_{inj,xy}$ is the lateral injection efficiency to account for leakage outside $A_{aperture}$, $\tau_{sp,B}$ is the spontaneous carrier (non-radiative and radiative) recombination lifetime in the barrier region, and τ_{cap} is the QW carrier capture time. For the thermionic emission process of i_{esc} and i_{leak} [15], $A_{0,A}$ and $A_{0,B}$ are the Richardson constants for the QWs and SCH, respectively, $E_{g,C}$ is the band gap for the cladding region, and η_{esc} and η_{leak} are ideality factors for the two processes. As the carrier concentration in the QWs is orders of magnitude larger than in the SCH, a more sophisticated (non-linear) model for the spontaneous carrier recombination is used, where well-known A-, B-, and C-coefficients for Schockley-Read-Hall-, radiative-, and Auger-recombination, respectively, are employed. For the stimulated carrier recombination rate, Γ is the optical confinement factor, ν_g is the group velocity, and g is the optical gain (material gain) in the QWs. The latter is modelled by the function:

$$g(n_A,S,T) = \left\{a_0(T) \cdot \ln\left(\frac{n_A/V_A + N_S}{N_0(T) + N_S}\right) - a_1 \cdot (\lambda(T) - \lambda_g(T)) - a_2 \cdot (\lambda(T) - \lambda_g(T))^2\right\} \left[\frac{1}{1 + \varepsilon \cdot S \cdot \Gamma/V_A}\right]. \tag{17}$$

where λ is the lasing (resonance) wavelength, λ_g is the peak gain wavelength, ε is the gain suppression factor with respect to photon density, and S is the number of photons in the optical resonator. N_0 represents the transparency carrier density (for $\lambda = \lambda_g$), N_S is the gain carrier density linearity factor [9], and a_0, a_1, and a_2 represent gain coefficients with respect to logarithmic carrier density-, linear wavelength-, and parabolic wavelength-dependency, respectively.

The coupled rate equation model can be translated into equivalent circuits that correspond to sub-circuit 2 and 3,

where the capacitors C_B and C_A [F] models the charge accumulation in the SCH and QWs, respectively, and where their voltage drop U_B and U_A [V] are set to represent n_B and n_A by $U_B \sim f_B \cdot n_B$ and $U_A \sim f_A \cdot n_A$. The circuit elements then become:

$$I_{inj} = q \cdot i_{inj}, \tag{18}$$

$$I_{sp,B} = q \cdot i_{sp,B}, \tag{19}$$

$$I_{cap} = q \cdot i_{cap}, \tag{20}$$

$$I_{esc} = q \cdot i_{esc}, \tag{21}$$

$$I_{leak} = q \cdot i_{leak}, \tag{22}$$

$$I_{sp,A} = q \cdot i_{sp,A}, \tag{23}$$

$$I_{st,A} = q \cdot i_{st}, \tag{24}$$

$$C_A = \frac{q}{f_A}, \tag{25}$$

$$C_B = \frac{q}{f_B}, \tag{26}$$

where f_B and f_A are scaling factors to adapt U_B and U_A to be in the same order of magnitude as the VCSEL voltage drop U to allow for convergence and higher accuracy in the circuit simulator.

C. Sub-Circuit 4: Photon Accumulation in Resonator

Sub-circuit 4 is used to trace the number of photons accumulated in the optical resonator, S. This allows for accounting for the effects of stimulated and spontaneous emission processes and resonator loss on VCSEL performance. Even though datacom VCSELs are commonly multimode, a single-mode approximation is made as it reduces model complexity considerably, and motivated by that these VCSELs will be operated at modulation frequencies that are far beyond the cut-off frequency for spatial hole burning effects [16].

The following single-mode rate equation is used to describe the change in S over time [9]:

$$\frac{dS}{dt} = i_{st} + i_{sp} - i_{abs} - i_{bm} - i_{tm}, \tag{27}$$

where i_{sp} is the rate of spontaneously emitted photons in the QWs that contribute to the number of photons in the lasing mode, i_{abs} is the loss rate of photons through free-carrier absorption in the doped distributed Bragg reflectors (DBRs), and i_{bm} and i_{tm} are the loss rates of photons through the bottom and top DBR, respectively. These rates are in turn modelled by:

$$i_{sp}(n_A,T) = \beta \cdot B(T) \cdot \frac{n_A^2}{V_A}, \tag{28}$$

$$i_{abs}(S,T) = \alpha_{abs}(T) \cdot S, \tag{29}$$

$$i_{bm}(S,T) = \alpha_{bm}(T) \cdot S, \tag{30}$$

$$i_{tm}(S,T) = \alpha_{tm}(T) \cdot S, \tag{31}$$

where β is the spontaneous emission coupling factor, α_{abs} is the free-carrier absorption coefficient, and α_{bm} and α_{tm} are the mirror out-coupling coefficient for the bottom and top DBR, respectively. The optical output power from the VCSEL, P_{opt} [W], is then obtained from:

$$P_{opt} = \frac{h \cdot c}{\lambda(T)} \cdot i_{tm}. \tag{32}$$

The rate equation model can be translated into an equivalent circuit that corresponds to sub-circuit 4, where the capacitor C_S [F] models the photon accumulation in the resonator, and where the voltage drop U_S [V] is set to represent S by $U_S \sim f_S \cdot S$. The circuit elements then become:

$$I_{st,S} = \eta \cdot q \cdot i_{st}, \quad (33)$$

$$I_{sp} = \eta \cdot q \cdot i_{sp}, \quad (34)$$

$$I_{abs} = \eta \cdot q \cdot i_{abs}, \quad (35)$$

$$I_{bm} = \eta \cdot q \cdot i_{bm}, \quad (36)$$

$$I_{tm} = \eta \cdot q \cdot i_{tm}, \quad (37)$$

$$C_S = \frac{\eta \cdot q}{f_S}, \quad (38)$$

where

$$\eta = \frac{h \cdot c}{q \cdot \lambda}, \quad (39)$$

and c is the speed of light, f_S is a scaling factor to adapt U_S to be in the same order of magnitude as the VCSEL voltage drop U, and the optical output power $P_{opt} \sim I_{tm}$.

D. Sub-Circuit 5: Internal Device Temperature

Sub-circuit 5 is used to trace the internal temperature of the VCSEL, T. This allows for accounting for the important effects of self-heating on VCSEL performance. The internal temperature can deviate strongly from the ambient temperature, T_{amb}. For example, at room-temperature ambient conditions the internal temperature is typically 100°C higher at the thermal rollover.

The following differential equation is used to describe the change in T [K] over time [17]:

$$\frac{\tau_{th}(T)}{r_{th}(T)} \cdot \frac{dT}{dt} = g_{gen} - g_{diss}, \quad (40)$$

where τ_{th} is the thermal time constant and r_{th} is the thermal impedance. g_{gen} and g_{diss} is the heat generation and dissipation power, respectively, and they are in turn modelled by:

$$g_{gen}(T) = U \cdot I - P_{opt}, \quad (41)$$

$$g_{diss}(T) = \frac{1}{r_{th}(T)} \cdot (T - T_{amb}). \quad (42)$$

The differential equation model can be translated into an equivalent circuit that corresponds to sub-circuit 5, where the capacitor C_T [F] models the heat build-up inside the device, and where the voltage drop U_T [V] is set to represent T by $U_T \sim f_T \cdot T$. The circuit elements then become:

$$I_{gen} = g_{gen}, \quad (43)$$

$$C_T = \frac{\tau_{th}}{r_{th} \cdot f_T}, \quad (44)$$

$$R_{th} = r_{th} \cdot f_T, \quad (45)$$

$$U_{amb} = T_{amb} \cdot f_T, \quad (46)$$

where f_T is a scaling factor to adapt U_T to be in the same order of magnitude as the VCSEL voltage drop U.

Temperature dependencies are included for the following material and device parameters, via first, second and third order derivatives around room temperature (RT), T_{RT} [K]:

$$r_m(T) = r_{m,RT} + \left.\frac{dr_m}{dT}\right|_{RT} \cdot (T - T_{RT}) + \frac{1}{2} \cdot \left.\frac{d^2 r_m}{dT^2}\right|_{RT} \cdot$$
$$(T - T_{RT})^2 + \frac{1}{6} \cdot \left.\frac{d^3 r_m}{dT^3}\right|_{RT} \cdot (T - T_{RT})^3 \quad (47)$$

$$E_{g,A}(T) = E_{g,A,RT} + \left.\frac{dE_{g,A}}{dT}\right|_{RT} \cdot (T - T_{RT}) \quad (48)$$

$$E_{g,B}(T) = E_{g,B,RT} + \left.\frac{dE_{g,B}}{dT}\right|_{RT} \cdot (T - T_{RT}) \quad (49)$$

$$E_{g,C}(T) = E_{g,C,RT} + \left.\frac{dE_{g,C}}{dT}\right|_{RT} \cdot (T - T_{RT}) \quad (50)$$

$$A(T) = A_{RT} + \left.\frac{dA}{dT}\right|_{RT} \cdot (T - T_{RT}) \quad (51)$$

$$B(T) = B_{RT} + \left.\frac{dB}{dT}\right|_{RT} \cdot (T - T_{RT}) +$$
$$\frac{1}{2} \cdot \left.\frac{d^2 B}{dT^2}\right|_{RT} \cdot (T - T_{RT})^2 \quad (52)$$

$$C(T) = C_{RT} + \left.\frac{dC}{dT}\right|_{RT} \cdot (T - T_{RT}) +$$
$$\frac{1}{2} \cdot \left.\frac{d^2 C}{dT^2}\right|_{RT} \cdot (T - T_{RT})^2 \quad (53)$$

$$a_0(T) = a_{0,RT} + \left.\frac{da_0}{dT}\right|_{RT} \cdot (T - T_{RT}) +$$
$$\frac{1}{2} \cdot \left.\frac{d^2 a_0}{dT^2}\right|_{RT} \cdot (T - T_{RT})^2 \quad (54)$$

$$N_0(T) = N_{0,RT} + \left.\frac{dN_0}{dT}\right|_{RT} \cdot (T - T_{RT}) \quad (55)$$

$$\lambda(T) = \lambda_{RT} + \left.\frac{d\lambda}{dT}\right|_{RT} \cdot (T - T_{RT}) \quad (56)$$

$$\lambda_g(n_A, T) = \lambda_{g,RT} + \left.\frac{d\lambda_g}{dT}\right|_{RT} \cdot (T - T_{RT}) +$$
$$\left.\frac{d\lambda_g}{d(n_A/V_A)}\right|_0 \cdot (n_A/V_A) + \frac{1}{2} \cdot \left.\frac{d^2\lambda_g}{d(n_A/V_A)^2}\right|_0 \cdot (n_A/V_A)^2$$
$$(57)$$

$$\alpha_{abs}(T) = \alpha_{abs,RT} + \left.\frac{d\alpha_{abs}}{dT}\right|_{RT} \cdot (T - T_{RT}) +$$
$$\frac{1}{2} \cdot \left.\frac{d^2 \alpha_{abs}}{dT^2}\right|_{RT} \cdot (T - T_{RT})^2 \quad (58)$$

$$\alpha_{bm}(T) = \alpha_{bm,RT} + \left.\frac{d\alpha_{bm}}{dT}\right|_{RT} \cdot (T - T_{RT}) \quad (59)$$

$$\alpha_{tm}(T) = \alpha_{tm,RT} + \left.\frac{d\alpha_{tm}}{dT}\right|_{RT} \cdot (T - T_{RT}) \quad (60)$$

$$r_{th}(T) = r_{th,RT} + \left.\frac{dr_{th}}{dT}\right|_{RT} \cdot (T - T_{RT}) \quad (61)$$

where r_m represents the total mesa resistance, see section III-A below. Note also the free carrier density dependence that is used for λ_g, to be able to account for the red-shift (band gap shrinkage) from many body effects [9].

III. DEMONSTRATION ON A 28-GHZ-BANDWIDTH VCSEL

To demonstrate the large-signal equivalent circuit, it is implemented in Keysight's Advanced Design System (ADS) software, and applied to an oxide-confined 850-nm-wavelength state-of-the-art high-speed VCSEL developed at Chalmers University of Technology [18]. It has a maximum bandwidth of 28 GHz at RT at a bias current of 9 mA.

A. VCSEL Design, Input Impedance Circuit, and Model Parameters

High-speed datacom VCSELs are based on [18], [19]: 1) SCH-design that mitigate carrier transport effects; 2) multiple QW design that enable high differential optical gain; 3) short effective resonator length for high optical confinement to the active region; and 4) contact pad and mesa layout that provide low parasitic capacitance. A low pad capacitance is usually obtained by planarizing the mesa structure by spin coating a thick low-κ dielectric layer before depositing the top pad. A low mesa capacitance is usually obtained by either proton implantation in the outer parts, or using a multiple oxide layer scheme, in the top mesa.

The design and performance of the 850-nm-wavelength 28-GHz-bandwidth VCSEL that is used for the demonstration has been thoroughly presented in [18]. In short, the epitaxial structure consists of a 74-nm-thick SCH containing five 4-nm-thick strained $In_{0.07}Ga_{0.93}As/Al_{0.37}Ga_{0.63}As$ QWs, a top p-doped DBR with 20 Bragg pairs of $Al_{0.12}Ga_{0.88}As/Al_{0.9}Ga_{0.1}As$, and a bottom n-doped DBR with five $Al_{0.12}Ga_{0.88}As/Al_{0.9}Ga_{0.1}As$ and 24 $Al_{0.12}Ga_{0.88}As/AlAs$ Bragg pairs. Fig. 3 illustrates the device layout, where benzocyclobutene is used as low-κ dielectric layer, and a multiple oxide layer structure is used in the top mesa. For this device, $A_{aperture}$ is approximately a circular area with a diameter of 7 μm, resulting in multimode operation.

Also included in Fig. 3 is the RLC-input impedance circuit (together with the voltage source for the SCH) that is used to represent the device specific layout, where the origin of the circuit elements are illustrated. L_b and R_b model the bond wire impedance, L_{p1}, R_{p1}, L_{p2}, R_{p2}, C_p, and R_{p3} represent the contact pad impedance, and C_{m1}, R_{m1}, C_{m2}, R_{m2}, C_{m3}, R_{m3} model the mesa impedance, acknowledging that the mesa has three regions with different oxide layer structures.

C_{dep} is used to represent the depletion capacitance of the SCH, outside $A_{aperture}$. This means that the total pin-junction capacitance of the SCH is modelled by the diffusion
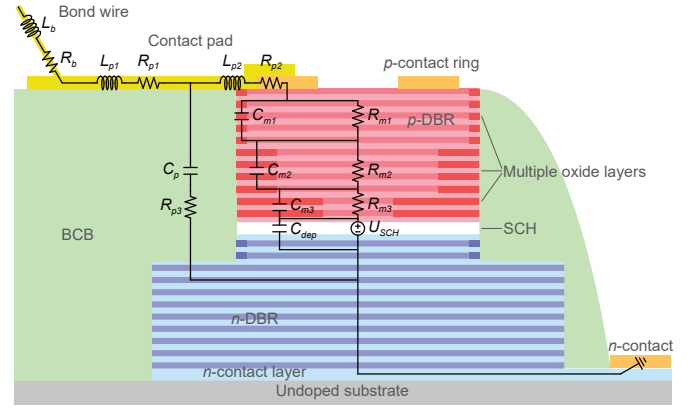

Fig. 3. Schematic cross-sectional view of the 28-GHz-bandwidth VCSEL, together with sub-circuit 1 that is used to model the input impedance and voltage drop over the SCH.

capacitance resulting from U_{SCH} (inside $A_{aperture}$) in parallel with the depletion capacitance C_{dep} (outside $A_{aperture}$). The diffusion capacitance will vary with drive current and temperature, while the depletion capacitance is approximated to be independent of drive current and temperature. This approximation is motivated by the high doping levels of the SCH claddings resulting in a thickness of the depletion region (outside $A_{aperture}$) that is close to the SCH thickness (d_B), independent of modulation conditions. Note that the total mesa resistance $r_m(T) = R_{m1} + R_{m2} + R_{m3}$ is strongly temperature dependent, as in (47), where $R_{m1} = \eta_{Rm1} \cdot r_m$, $R_{m2} = \eta_{Rm2} \cdot r_m$ and $R_{m3} = \eta_{Rm3} \cdot r_m$.

The values for the material and device parameters that are needed in the model are either obtained from literature, measurements, or supplied by the VCSEL designers, via extraction from their 2D/3D physics-based optical-electrical-thermal device simulation tools and material gain calculators. The more uncertain parameter values have been fine-tuned for better agreement between simulations and measurements. In this process, the fitting was made to measured static current-power-voltage-characteristics, wavelength shift with current, and frequency dependent S_{11}- and S_{21}-parameters, at different ambient temperatures. After this fine-tuning to measured static and small-signal data, the model parameter values were fixed. Thus, no fine-tuning (fitting) was done to measured large-signal data (e.g. electrical eye diagrams in section III-D, Figures 7 and 8). Tables I, II, III, IV, V, VI and VII list the final values of the parameters used for the high-speed VCSEL, also indicating their origin and if they were fine-tuned to measured static and small-signal data. Particularly important are the ones for the material gain model, see (17), as the VCSEL performance, and how it varies with temperature, is very sensitive to the active region gain properties (i.e. absolute gain, differential gain, and detuning between gain peak wavelength and VCSEL resonance wavelength).

B. VCSEL Steady-State Characteristics

The DC simulation component in ADS was applied to obtain the VCSEL steady-state characteristics, where an ideal

TABLE I
DEVICE GEOMETRY PARAMETERS USED FOR THE 28-GHZ-BANDWIDTH VCSEL.

Parameter	Symbol	Unit	Value	Origin	Fine-tuned
Number of QWs	n_{QW}	-	5	Design	-
Thickness QW	d_{QW}	m	$4.0 \cdot 10^{-9}$	Design	-
Thickness SCH	d_B	m	$74.0 \cdot 10^{-9}$	Design	-
Current confinement aperture area SCH	$A_{aperture}$	m^2	$38.5 \cdot 10^{-12}$	Design	-

[1] Primarily for IPV fit   [2] Primarily for S_{11} fit   [3] Primarily for S_{21} fit

TABLE II
INPUT IMPEDANCE PARAMETERS USED FOR THE 28-GHZ-BANDWIDTH VCSEL.

Parameter	Symbol	Unit	Value	Origin	Fine-tuned
Bond wire inductance	L_b	H	0	No bond wire	-
Bond wire resistance	R_b	Ω	0	No bond wire	-
Bond pad inductance 1	L_{p1}	H	$76.0 \cdot 10^{-12}$	-	Yes[2]
Bond pad resistance 1	R_{p1}	Ω	0	-	-
Bond pad inductance 2	L_{p2}	H	0	-	-
Bond pad resistance 2	R_{p2}	Ω	0	-	-
Bond pad capacitacne	C_p	F	$50.0 \cdot 10^{-15}$	-	Yes[2]
Bond pad resistance 3	R_{p3}	Ω	15.0	-	Yes[2]
Mesa resistance @ RT	r_m	Ω	170	Simulations	Yes[2]
Mesa resistance linear temp. coeff. @ RT	dr_m/dT	Ω/K	-0.96	Simulations	Yes[2]
Mesa resistance quadratic temp. coeff. @ RT	$d^2 r_m/dT^2$	Ω/K^2	$1.38 \cdot 10^{-2}$	Simulations	Yes[2]
Mesa resistance cubic temp. coeff. @ RT	$d^3 r_m/dT^3$	Ω/K^3	$-1.11 \cdot 10^{-4}$	Simulations	Yes[2]
Mesa resistance 1 factor	η_{Rm1}	-	0.285	Simulations	-
Mesa resistance 2 factor	η_{Rm2}	-	0.125	Simulations	-
Mesa resistance 3 factor	η_{Rm3}	-	0.590	Simulations	-
Mesa capacitance 1	C_{m1}	F	$2.02 \cdot 10^{-15}$	Simulations	-
Mesa capacitance 2	C_{m2}	F	$19.5 \cdot 10^{-15}$	Simulations	-
Mesa capacitance 3	C_{m3}	F	$88.6 \cdot 10^{-15}$	Simulations	-
Depletion capacitance	C_{dep}	F	$50.0 \cdot 10^{-15}$	Simulations	-

[1] Primarily for IPV fit   [2] Primarily for S_{11} fit   [3] Primarily for S_{21} fit

TABLE III
SCH REGION PARAMETERS USED FOR THE 28-GHZ-BANDWIDTH VCSEL.

Parameter	Symbol	Unit	Value	Origin	Fine-tuned
Bandgap SCH @ RT	$E_{g,B,RT}$	eV	1.89	Literature	Yes[1]
Bandgap SCH linear temp. coeff. @ RT	$dE_{g,B}/dT$	eV/K	$-4.5 \cdot 10^{-4}$	Literature	Yes[1]
Electron relative effective mass SCH	$m_{e,B}$	-	0.0977	Literature	-
Heavy hole relative effective mass SCH	$m_{hh,B}$	-	0.596	Literature	-
Injection efficiency lateral direction SCH	$\eta_{inj,xy}$	-	0.8	Simulations	-
Spontaneous carrier recombination lifetime SCH	$\tau_{sp,B}$	s	$5.0 \cdot 10^{-9}$	Literature	-
Ideality factor recombination current SCH	η_B	-	1.0	Literature	Yes[1]
Ideality factor leakage current SCH	η_{leak}	-	2.0	Literature	Yes[1]
Richardson constant SCH	$A_{0,B}$	A/m^2/K^2	$7.4 \cdot 10^5$	Literature	Yes[1]
Bandgap cladding @ RT	$E_{g,C}$	eV	2.31	Literature	Yes[1]
Bandgap cladding linear temp. coeff. @ RT	$dE_{g,C}/dT$	eV/K	$4.94 \cdot 10^{-4}$	Literature	Yes[1]

[1] Primarily for IPV fit   [2] Primarily for S_{11} fit   [3] Primarily for S_{21} fit

current source was used to drive the VCSEL. To mimic the measurement setup, a very simple equivalent circuit was implemented in ADS to represent the photodetector, consisting of a current source connected to an ideal 50 Ω output terminal. The current is $I_{det} = \eta_{det} \cdot R \cdot P_{opt}$ where η_{det} is the optical coupling efficiency and R [A/W] is the responsivity of the photodetector. Results on simulated VCSEL voltage drop, optical output power, and resonance wavelength shift, versus drive current at three different ambient temperatures are shown in Fig. 4a, 4c and 4d and are in good agreement with corresponding measurement data. For the measured wavelength shift, the fundamental (LP$_{01}$) mode was traced.

Fig. 4b displays the simulated internal temperature, which fits well with the measured internal temperature that was indirectly obtained from extracting the dissipated power from measured IPV-characteristics and the thermal impedance from resonance wavelength shift with dissipated power and ambient temperature [20]. The coefficient of determination R^2 for the data in Fig. 4a, 4b, 4c and 4d, averaged over the three ambient temperatures, is 0.9987, 0.9958, 0.9987 and 0.9946, respectively.

The non-linear behavior of the voltage drop with drive current required the use of a temperature dependent mesa resistance, r_m, which includes not only the second- but also

TABLE IV
ACTIVE REGION PARAMETERS USED FOR THE 28-GHZ-BANDWIDTH VCSEL.

Parameter	Symbol	Unit	Value	Origin	Fine-tuned
Effective bandgap QW @ RT	$E_{g,A,RT}$	eV	1.53	Literature	Yes[1]
Effective bandgap QW linear temp. coeff. @ RT	$dE_{g,A}/dT$	eV/K	$-1.63 \cdot 10^{-3}$	Literature	Yes[1]
Electron relative effective mass QW	$m_{e,A}$	-	0.0622	Literature	-
Heavy hole relative effective mass QW	$m_{hh,A}$	-	0.346	Literature	-
Carrier capture time QW	τ_{cap}	s	$7.0 \cdot 10^{-12}$	Literature	Yes[3]
Ideality factor recombination current QW	η_A	-	1.6	Literature	Yes[1]
Ideality factor leakage current QW	η_{esc}	-	2.0	Literature	Yes[1]
Richardson constant QW	$A_{0,A}$	A/m^2/K^2	$7.4 \cdot 10^5$	Literature	Yes[1]
Shockley–Read–Hall recombination coeff. QW @ RT	A_{RT}	1/s	$0.45 \cdot 10^9$	Literature	-
Shockley–Read–Hall recombination coeff. QW linear temp. coeff. @ RT	dA/dT	1/s/K	0	Literature	-
Shockley–Read–Hall recombination coeff. QW quadratic temp. coeff. @ RT	d^2A/dT^2	1/s/K^2	0	Literature	-
Bimolecular recombination coeff. QW @ RT	B_{RT}	m^3/s	$3.0 \cdot 10^{-16}$	Calculations	-
Bimolecular recombination coeff. QW linear temp. coeff. @ RT	dB/dT	m^3/s/K	$-1.19 \cdot 10^{-18}$	Calculations	-
Bimolecular recombination coeff. QW quadratic temp. coeff. @ RT	d^2B/dT^2	m^3/s/K^2	$5.74 \cdot 10^{-21}$	Calculations	-
Auger recombination coeff. QW @ RT	C_{RT}	m^6/s	$-7.9 \cdot 10^{-42}$	Literature	-
Auger recombination coeff. QW linear temp. coeff. @ RT	dC/dT	m^6/s/K	$8.2 \cdot 10^{-44}$	Literature	-
Auger recombination coeff. QW quadratic temp. coeff. @ RT	d^2C/dT^2	m^6/s/K^2	$-5.4 \cdot 10^{-46}$	Literature	-

[1] Primarily for IPV fit   [2] Primarily for S_{11} fit   [3] Primarily for S_{21} fit

TABLE V
QW MATERIAL GAIN PARAMETERS USED FOR THE 28-GHZ-BANDWIDTH VCSEL.

Parameter	Symbol	Unit	Value	Origin	Fine-tuned
Gain logarithmic carrier density coeff. @ RT	$a_{0,RT}$	1/m	$7.54 \cdot 10^5$	Calculations	-
Gain logarithmic carrier density linear temp. coeff. @ RT	da_0/dT	1/m/K	$8.22 \cdot 10^2$	Calculations	-
Gain logarithmic carrier density quadratic temp. coeff. @ RT	d^2a_0/dT^2	1/m/K^2	2.66	Calculations	-
Gain linear wavelength coeff. (when $\lambda \leq \lambda_g$)	a_1	1/m^2	$-1.4 \cdot 10^{13}$	Calculations	-
Gain parabolic wavelength coeff. (when $\lambda \leq \lambda_g$)	a_2	1/m^3	$1.57 \cdot 10^{20}$	Calculations	-
Gain linear wavelength coeff. (when $\lambda > \lambda_g$)	a_1	1/m^2	$-1.34 \cdot 10^{13}$	Calculations	-
Gain parabolic wavelength coeff. (when $\lambda > \lambda_g$)	a_2	1/m^3	$2.03 \cdot 10^{21}$	Calculations	-
Gain transparency carrier density @ RT	$N_{0,RT}$	1/m^3	$2.76 \cdot 10^{24}$	Calculations	-
Gain transparency carrier density linear temp. coeff. @ RT	dN_0/dT	1/m^3/K	$9.22 \cdot 10^{21}$	Calculations	-
Gain carrier density linearity factor	N_S	1/m^3	$-1.5 \cdot 10^{21}$	Calculations	-
Gain suppression factor	ε	m^3	$5.0 \cdot 10^{-24}$	Literature	Yes[3]
Gain peak wavelength @ RT and zero carrier density	$\lambda_{g,RT}$	m	$857.0 \cdot 10^{-9}$	Measurements	-
Gain peak wavelength linear temp. coeff. @ RT	$d\lambda_g/dT$	m/K	$0.314 \cdot 10^{-9}$	Calculations	-
Gain peak wavelength linear carrier density coeff. @ RT	$d\lambda_g/d(n_A/V_A)$	m^4	$-3.26 \cdot 10^{-33}$	Calculations	-
Gain peak wavelength quadratic carrier density coeff. @ RT	$d^2\lambda_g/d(n_A/V_A)^2$	m^7	$-5.44 \cdot 10^{-60}$	Calculations	-

[1] Primarily for IPV fit   [2] Primarily for S_{11} fit   [3] Primarily for S_{21} fit

TABLE VI
OPTICAL RESONATOR PARAMETERS USED FOR THE 28-GHZ-BANDWIDTH VCSEL.

Parameter	Symbol	Unit	Value	Origin	Fine-tuned
Resonance wavelength @ RT	λ_{RT}	m	$847.3 \cdot 10^{-9}$	Measurements	-
Resonance wavelength linear temp. coeff. @ RT	$d\lambda/dT$	m/K	$0.064 \cdot 10^{-9}$	Measurements	-
Group velocity	ν_g	m/s	$1.0 \cdot 10^8$	Simulations	-
Optical confinement factor QWs	Γ	-	$3.28 \cdot 10^{-2}$	Simulations	-
Spontaneous emission coupling factor	β	-	$4.68 \cdot 10^{-2}$	Literature	Yes[1]
Optical loss rate absorption @ RT	$\alpha_{abs,RT}$	1/s	$6.19 \cdot 10^{10}$	Simulations	Yes[1]
Optical loss rate absorption linear temp. coeff. @ RT	$d\alpha_{abs}/dT$	1/s/K	0	Simulations	Yes[1]
Optical loss rate absorption quadratic temp. coeff. @ RT	$d^2\alpha_{abs}/dT^2$	1/s/K^2	$5.0 \cdot 10^6$	Simulations	Yes[1]
Optical loss rate bottom mirror @ RT	$\alpha_{bm,RT}$	1/s	$1.35 \cdot 10^{10}$	Simulations	-
Optical loss rate bottom mirror linear temp. coeff. @ RT	$d\alpha_{bm}/dT$	1/s/K	$-3.1 \cdot 10^7$	Simulations	-
Optical loss rate top mirror @ RT	$\alpha_{tm,RT}$	1/s	$1.91 \cdot 10^{11}$	Simulations	-
Optical loss rate top mirror linear temp. coeff. @ RT	$d\alpha_{tm}/dT$	1/s/K	$-2.66 \cdot 10^8$	Simulations	-

[1] Primarily for IPV fit   [2] Primarily for S_{11} fit   [3] Primarily for S_{21} fit

TABLE VII
DEVICE HEATING PARAMETERS USED FOR THE 28-GHZ-BANDWIDTH VCSEL.

Parameter	Symbol	Unit	Value	Origin	Fine-tuned
Device thermal time constant	τ_{th}	s	$1.0 \cdot 10^{-7}$	Literature	-
Device thermal impedance @ RT	$r_{th,RT}$	K/W	$2.8 \cdot 10^{3}$	Measurements	-
Device thermal impedance linear temp. coeff. @ RT	$dr_{th,RT}/dT$	1/W	2.5	Measurements	Yes[1]

[1] Primarily for IPV fit   [2] Primarily for S_{11} fit   [3] Primarily for S_{21} fit
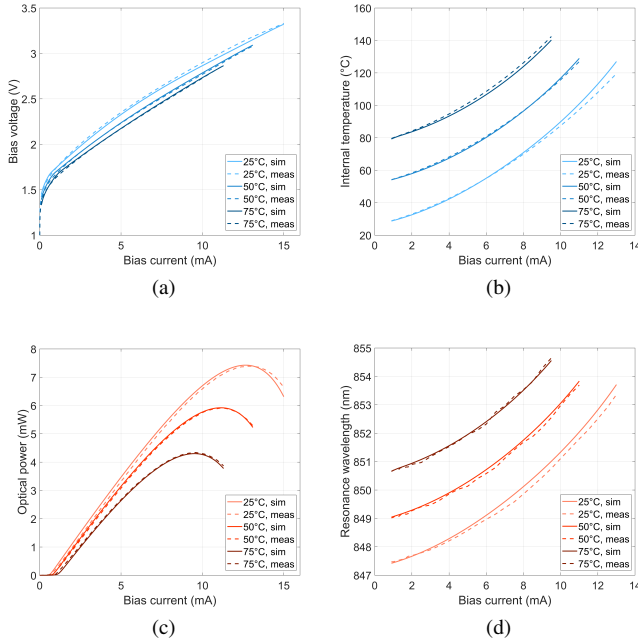
Fig. 4. Measured (dashed lines) and simulated (solid lines) VCSEL steady-state characteristics: (a) voltage drop; (b) internal temperature; (c) optical output power; and (d) resonance wavelength (LP$_{01}$-mode), as a function of drive current at three different ambient temperatures.

the third-order derivative on temperature, see (47). In addition, to get good agreement in the optical output power around the thermal roll-over involved fine-tuning the temperature dependent carrier escape and leakage processes (i_{esc} and i_{leak}, in (13) and (14)) via parameters $A_{0,A}$, η_{esc}, $A_{0,B}$ and η_{leak}. Finally, to match the resonance wavelength shift versus drive current, the linear temperature coefficient of the thermal impedance was fine-tuned. Note that in the optical output power measurements it is critical that all output power from the VCSEL is captured by the photodetector (or that η_{det} is precisely known), wherefore a calibrated integrating sphere was used. Similarly, in the voltage measurements it is important that the actual VCSEL voltage is monitored, wherefore a four-probe technique was applied.

C. VCSEL Small-Signal Modulation Characteristics

The S-parameter simulation component in ADS was applied to obtain the VCSEL small-signal modulation characteristics, where an ideal current source was used to bias the VCSEL and an ideal 50 Ω input terminal was used to supply the modulation voltage to the VCSEL. They were combined using an ideal bias-T. To mimic the measurement setup, the simple

equivalent circuit for the photodetector used for the steady-state simulations was complemented with an ideal bias tee for AC-coupling to the ideal 50 Ω output terminal.

Fig. 5 shows simulated S_{11}- and S_{21}-parameters (for modulation frequencies up to 40 GHz) for the VCSEL versus bias current, I_b, at two different ambient temperatures, and are in fair agreement with corresponding measurements. The coefficient of determination R^2 for the data in Fig. 5a, 5b, 5c and 5d, averaged over the seven bias currents, is 0.83526/0.96914 (real/imaginary part), 0.75387/0.92353 (real/imaginary part), 0.9166 (linear magnitude) and 0.96807 (linear magnitude), respectively.

To get a fair match in S_{11} required to fine-tune the contact pad circuit elements (L_{p1}, R_{p1}, L_{p2}, R_{p2}, C_p, and R_{p3}). Moreover, a fair match in S_{21} involved fine-tuning the QW carrier capture time, τ_{cap}, and the gain suppression factor, ε. Note that for the measured S_{21}, the bandwidth-limited response of the photodetector was subtracted to yield the actual S_{21} for the VCSEL. In Fig. 5, a small off-set in S_{11}, and a small deviation in S_{21} magnitude at the lowest bias currents, can be noted. We believe this off-set in S_{11} can be reduced by including temperature dependence of the mesa capacitances (C_{m1}, C_{m2}, C_{m3}) and/or depletion capacitance (C_{dep}) and that the deviation in S_{21} magnitude at the lowest bias currents can be decreased by further refining the material gain model (in (17)) for the QWs.

D. Link Large-Signal Response

The large-signal equivalent circuit for the VCSEL is here demonstrated in a back-to-back link configuration. The transient simulation component in ADS was applied to compute the large-signal time-response under OOK and PAM4 modulation for the link, where an ideal current source was used to bias the VCSEL and an ideal 50 Ω time-domain Voltage Source with a Pseudo-Random Bit Sequence (VTPRBS) followed by a Butterworth filter was used to supply the modulation voltage to the VCSEL. They were combined using an ideal bias-T. The rise- and fall-time of the VTPRBS was set to 7 ps and 30 ps for the OOK- and PAM4-modulation, respectively, and the bandwidth of the Butterworth filter was set to 50 GHz. This was to mimic the limitations of the pattern generator used for the link measurements. Fig. 6 shows simulated 28 Gbaud OOK and PAM4 eye diagrams for an ideal 50 Ω load (instead of the VCSEL) and with a peak-to-peak modulation voltage, V_{pp}, of 380 and 675 mV, respectively, after these VTPRBS settings, with good agreement to corresponding measured eye diagrams. A pseudo-random bit sequence (PRBS) of length $2^{15} - 1$ was selected for all measured eye diagrams to have
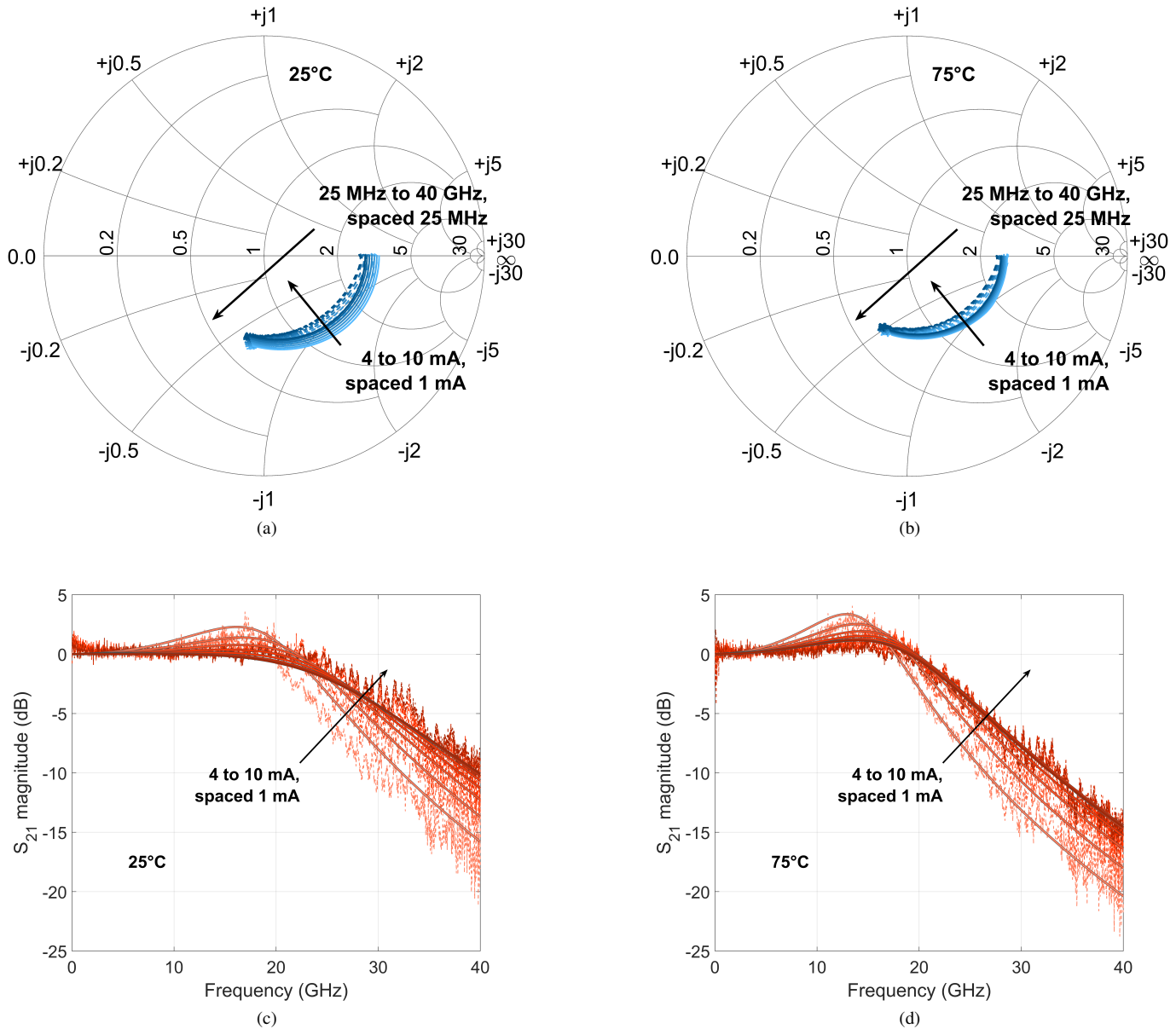
Fig. 5. Measured (dashed lines) and simulated (solid lines) S-parameters for the VCSEL: (a) Smith chart with complex S_{11} at 25°C; (b) Smith chart with complex S_{11} at 75°C; (c) squared magnitude of S_{21} at 25°C, normalized; and (d) squared magnitude of S_{21} at 75°C, normalized, as a function of modulation frequency and bias current.

a reasonable calculation time for the corresponding simulated eye diagrams.

To mimic the receiver end of the link, the equivalent circuit for the photodetector used for the small-signal simulations was complemented with a power amplifier between the current source and the bias-T. To account for the bandwidth limitations of both the photodetector and the amplifier, two low-pass filters (programmed to have a frequency response as specified in their respective datasheets) were also added. Note that an initial transient time, related to the thermal time constant, τ_{th}, is needed for the temperature inside the VCSEL to quasi-stabilize from a large-signal modulation that starts at time zero. Thus, for all simulated eye diagrams, the simulation data during this initial transient time were omitted. Fig. 7 and 8 show the results on simulated link 28 Gbaud eye diagrams for OOK- and

PAM4-modulation, respectively, at two different bias currents and two different ambient temperatures for the VCSEL, and are in good agreement with corresponding measured eye diagrams. Thus, a good match between simulated and actual VCSEL large-signal characteristics is obtained for the link.

IV. CONCLUSION

A large-signal equivalent circuit that can reproduce the optical waveforms generated by a high-speed datacom VCSEL under different modulation conditions has been developed, with purpose of facilitating the co-design of the VCSEL with the sophisticated driver and receiver electronics that is needed in next generation OIs. For the circuit to accurately predict the strongly varying VCSEL input and output characteristics with ambient temperature, drive current, and modulation frequency,
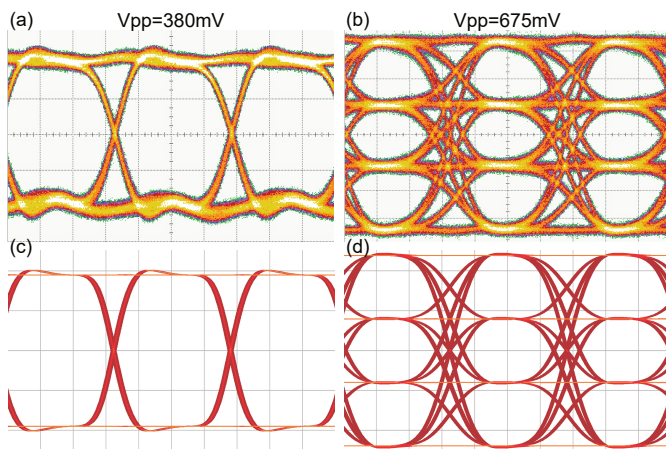
Fig. 6. Input electrical eye diagrams at 28 Gbaud with an ideal 50 Ω load: (a) measured, OOK-modulation; (b) measured, PAM4-modulation; (c) simulated, OOK-modulation; and (d) simulated, PAM4-modulation.

it consists of five interdependent sub-circuits requiring a self-consistent solution. To verify the circuit, it was implemented in ADS and applied to a 28-GHz-bandwidth 850-nm-wavelength VCSEL. Several physical parameters were needed to determine the circuit elements, where many were supplied by the VCSEL designers and some needed fine-tuning to better match simulated to measured steady-state and small-signal behavior. Eye diagrams were thereafter computed for a back-to-back link operating at 28 Gbaud OOK and PAM4 modulation at different ambient temperatures and bias currents, showing good agreement with measured eye diagrams. This indicates that the circuit, which is based on relatively simple physical models, can well predict the datacom VCSEL behavior under large-signal modulation at varying operating conditions without interpolating the behavior between different ambient temperatures. For datacom VCSELs the relative intensity noise (RIN) spectrum is also important, especially under higher-order-level modulation. To compute this, noise in the equivalent circuit elements needs to be included and related to the noise in the physical processes. This is left for future work.

REFERENCES

[1] D. Mahgerefteh and C. Thompson, "Techno-economic Comparison of Silicon Photonics and Multimode VCSELs," in *Opt. Fiber Commun. Conf.*, vol. 34, no. 2. Washington, D.C.: OSA, 2015, p. M3B.2.

[2] Ethernet Alliance, "Ethernet Roadmap 2020," 2020, (Accessed 4-Dec-2020). [Online]. Available: https://ethernetalliance.org/technology/2020-roadmap/

[3] J. Lavrencik, V. A. Thomas, S. Varughese, and S. E. Ralph, "DSP-Enabled 100 Gb/s PAM-4 VCSEL MMF Links," *J. Light. Technol.*, vol. 35, no. 15, pp. 3189–3196, Aug. 2017.

[4] A. Grabowski, J. Gustavsson, Z. S. He, and A. Larsson, "Large-Signal Circuit Model for Datacom VCSELs," in *2018 IEEE Int. Semicond. Laser Conf.* IEEE, Sep. 2018, pp. 1–2.

[5] S. Li, M. S. Nezami, D. Rolston, and O. Liboiron-Ladouceur, "A Compact High-Efficient Equivalent Circuit Model of Multi-Quantum-Well Vertical-Cavity Surface-Emitting Lasers for High-Speed Interconnects," *Appl. Sci.*, vol. 10, no. 11, p. 3865, Jun. 2020.

[6] M. Bou Sanayeh, W. Hamad, and W. Hofmann, "Equivalent Circuit Model of High-Performance VCSELs," *Photonics*, vol. 7, no. 1, p. 13, Jan. 2020.

[7] J. Yan, J. Wang, C. Tang, X. Liu, G. Zhang, and Y. He, "An Electrooptothermal-Coupled Circuit-Level Model for VCSELs Under Pulsed Condition," *IEEE Trans. Ind. Electron.*, vol. 66, no. 2, pp. 1315–1324, Feb. 2019.

[8] K. Szczerba and C. Kocot, "Behavioral modeling of VCSELs for high-speed optical interconnects," in *Vertical-Cavity Surface-Emitting Lasers XXII*, K. D. Choquette and C. Lei, Eds., vol. 1055204, no. 1. SPIE, Feb. 2018, p. 3.

[9] L. A. Coldren, S. W. Corzine, and M. L. Mašanović, *Diode Lasers and Photonic Integrated Circuits*, 2nd ed. Hoboken, NJ, USA: John Wiley & Sons, Inc., Mar. 2012, vol. 218.

[10] J. Wang, R. Murty, Z.-W. Feng, S-J. Taslim, A. Sridhara, X. Cai, A. Harren, N. Leong, G.-H. Koh, A.-N. Cheng, D. Dolfi, J. Chu, and L. Giovane, "100Gb/s PAM4 oxide VCSEL development progress at Broadcom," in *Vertical-Cavity Surface-Emitting Lasers XXIV*, C. Lei and L. A. Graham, Eds., no. February 2020. SPIE, Feb. 2020, p. 14.

[11] N. Ledentsov, Ł. Chorchos, V. Shchukin, V. Kalosha, J. P. Turkiewicz, and N. N. Ledentsov, "Development of VCSELs and VCSEL-based Links for Data Communication beyond 50Gb/s," in *Opt. Fiber Commun. Conf. 2020.* OSA, 2020, p. M2A.3.

[12] H.-L. Wang, W. Fu, J. Qiu, and M. Feng, "850 nm VCSELs for 50 Gb/s NRZ Error-Free Transmission over 100-meter OM4 and up to 115 °C Operation," in *Opt. Fiber Commun. Conf. 2019.* OSA, 2019, p. W3A.1.

[13] N. G. Nilsson, "An Accurate Approximation of the Generalized Einstein Relation for Degenerate Semiconductors," *Phys. Status Solidi*, vol. 19, no. 1, pp. K75–K78, Sep. 1973.

[14] D. McDonald and R. O'Dowd, "Comparison of Two- and Three-Level Rate Equations in the Modeling of Quantum-Well Lasers," *IEEE J. Quantum Electron.*, vol. 31, no. 11, pp. 1927–1934, 1995.

[15] S. M. Sze and K. K. Ng, *Physics of Semiconductor Devices*, 3rd ed. Wiley, 2007.

[16] J. Gustavsson, Å. Haglund, C. Carlsson, J. Bengtsson, and A. Larsson, "Harmonic and Intermodulation Distortion in Oxide-Confined Vertical-Cavity Surface-Emitting," *IEEE J. Quantum Electron.*, vol. 39, no. 8, pp. 941–951, Aug. 2003.

[17] P. Mena, J. Morikuni, S.-M. Kang, A. Harton, and K. Wyatt, "A Simple Rate-Equation-Based Thermal VCSEL Model," *J. Light. Technol.*, vol. 17, no. 5, pp. 865–872, May 1999.

[18] P. Westbergh, R. Safaisini, E. Haglund, J. S. Gustavsson, A. Larsson, and A. Joel, "High-speed 850 nm VCSELs with 28 GHz modulation bandwidth for short reach communication," in *Vertical-Cavity Surface-Emitting Lasers XVII*, K. D. Choquette and J. K. Guenter, Eds., vol. 8639, no. 0, Mar. 2013, p. 86390X.

[19] A. Larsson, "Advances in VCSELs for Communication and Sensing," *IEEE J. Sel. Top. Quantum Electron.*, vol. 17, no. 6, pp. 1552–1567, Nov. 2011.

[20] M. Daubenschüz and R. Michalzik, "Parameter extraction from temperature-dependent light-current-voltage data of vertical-cavity surface-emitting lasers," in *Proc. SPIE*, K. Panajotov, M. Sciamanna, A. Valle, and R. Michalzik, Eds., no. April 2016, Apr. 2016, p. 98920R.
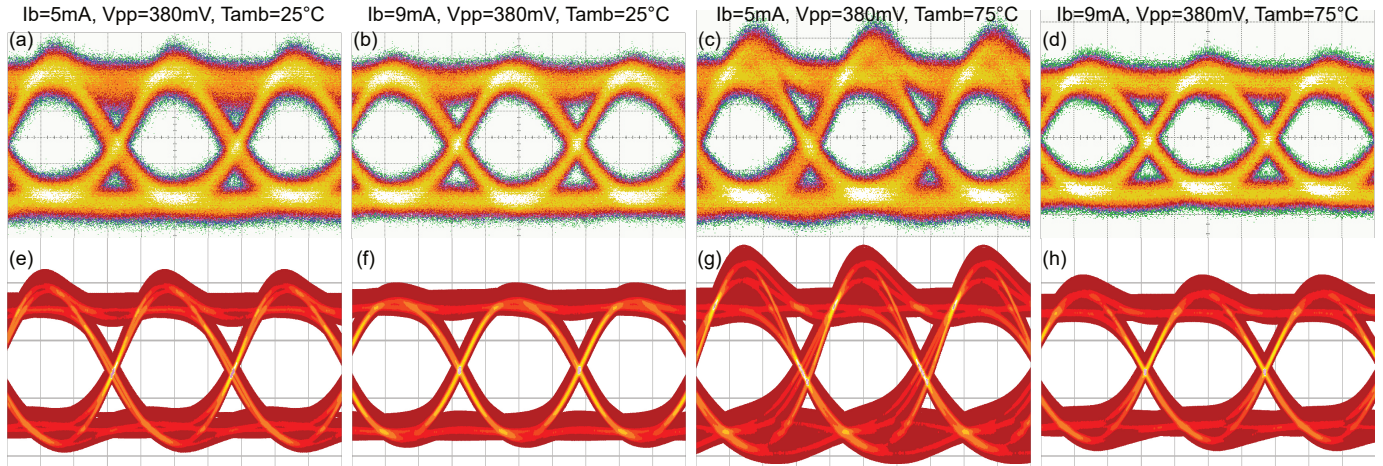
Fig. 7. Receiver electrical eye diagrams at 28 Gbaud OOK-modulation for the link at fixed modulation voltage and at two different bias currents and two different ambient temperatures for the VCSEL: (a)-(d) measured; and (e)-(h) simulated. For the simulated eye diagrams, the ADS density plot function was applied with 12 colors ranging from dark red (lowest density) to light purple (highest density).
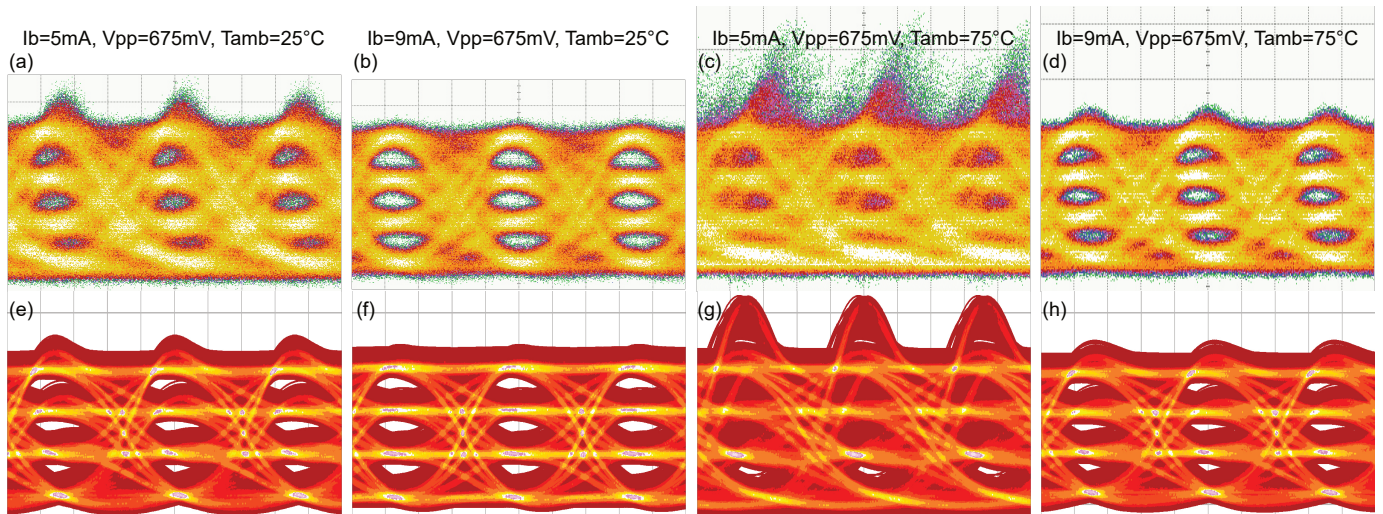

Fig. 8. Receiver electrical eye diagrams at 28 Gbaud PAM4-modulation for the link at fixed modulation voltage and at two different bias currents and two different ambient temperatures for the VCSEL: (a)-(d) measured; and (e)-(h) simulated. For the simulated eye diagrams, the ADS density plot function was applied with 12 colors ranging from dark red (lowest density) to light purple (highest density).